Chimica Techno Acta
published by Ural Federal University
eISSN 2411-1414; chimicatechnoacta.ru

ARTICLE
2022, vol. 9(4), No. 20229411
DOI: 10.15826/chimtech.2022.9.4.11

Structure and microwave dielectric properties of Bi- and Ge-doped calcium molybdate

Zoya A. Mikhaylovskaya [ab *], Elena S. Buyanova [ab], Sofia A. Petrova [c], Elizaveta A. Pankrushina [a], Alexander I. Malkin [d], Alexey N. Korotkov [d], Nikolay S. Knyazev [d]

a: Zavaritsky Institute of Geology and Geochemistry, Ural Branch of the Russian Academy of Sciences, Ekaterinburg 620110, Russia
b: Institute of Natural Sciences and Mathematics, Ural Federal University, Ekaterinburg 620026, Russia
c: Institute of Metallurgy, Ural Branch of the Russian Academy of Sciences, Ekaterinburg 620016, Russia
d: Engineering School of Information Technologies, Telecommunications and Control Systems, Ural Federal University, Ekaterinburg 620078, Russia
* Corresponding author: zozoikina@mail.ru

This paper belongs to a Regular Issue.

Abstract

The powders of $Ca_{1-2x}Bi_{2x}Mo_{1-x}Ge_xO_4$ solid solutions were synthesized by the conventional solid state method and investigated by X-ray powder diffraction and Raman spectroscopy. The $Ca_{1-2x}Bi_{2x}Mo_{1-x}Ge_xO_4$ compositions crystallize in scheelite structure (sp. gr. $I4_1/a$) at $0 \leq x \leq 0.4$, but traces of bismuth germanates are detected by scanning electron microscopy. The $x = 0.5$ composition contains several phases with $BiVO_4$- type structures. Raman spectroscopy detected the deformation of $[BO_4]^{2-}$ polyhedra and changes in B–O bond length (B = Mo, Ge). The energy gaps were calculated from the diffuse scattering spectra by the Kubelka-Munk method. Energy gap (E_g) values decrease with x from 3.29 eV to 2.91 eV, probably due to $6s^2$ electrons of bismuth in the valence band and changes of the conductivity band by electrons of germanium. Such values of E_g can provide photocatalytical activity of powders under UV and visible light. The electrodynamic parameters of the ceramic sample of $Ca_{1-2x}Bi_{2x}Mo_{1-x}Ge_xO_4$ were measured by the transmission line method. The average permittivity increases with x from ~10 to ~18 which correlates with theoretical ε, V_{mol} and total polarizability of samples. An increase in the concentration of bismuth and germanium leads to the additional resonant peaks in the spectra of ε, S_{11} and S_{21}. These resonant peaks can be probably caused by the appearance of irregular structural domains of Bi atoms or induced by the increased size of grains in the ceramic samples.

Keywords

calcium molybdate
bismuth molybdate
microwave dielectrics
Raman spectroscopy
energy gap

Received: 18.07.22
Revised: 04.08.22
Accepted: 04.08.22
Available online: 23.08.22

1. Introduction

Scheelite-type compounds include several groups of complex oxides with general formulae ABO_4. Not distorted scheelite type compounds crystallize in a tetragonal structure with a space group $I4_1/a$. Such compounds attracted much attention in the recent decades due to their multifunctional applications as microwave dielectric materials (i.e. the materials for wireless communication) [1–4], pigments and photocatalysts [5, 6], etc. $CaMoO_4$-based compounds also crystallize in the scheelite-type structure. The parent compound $CaMoO_4$ showed a relatively low permittivity and a high quality factor ($\varepsilon_r = 11.7$, $Q{\cdot}f = 55.000$, $\tau_f = -60$ ppm/°C) [3]. Doping of $CaMoO_4$ modifies its physical and chemical properties. For example, the isolated electron pair of bismuth provides a significant polarizability of Bi ions because doping by Bi^{3+} ions leads to the increase in ε [7–8] and at the same time – the decrease of the energy gap [9]. Thus, doping by Bi ions is a good instrument for regulating such parameters of the material. Substitution of A^{2+} by A^{3+} ions in ABO_4 can be realized in the following ways: (i) formation of additional interstitial oxygen position [10], (ii) formation of cationic vacancies [9], (iii)

codoping by A^+ [11] or by $B^{+3\cdots+5}$ [3]. The last way results in solid solutions with the general formulae $A_{1-x}Bi_xB_{1-x}Me_xO_4$ in the case of Me = B^{+5} or those with the general formulae $A_{1-2x}Bi_{2x}B_{1-x}Me_xO_4$, in the case of Me = B^{+4}. $A_{1-x}Bi_xB_{1-x}Me_xO_4$ compositions are relatively well investigated in the case of M = V [3, 6–9], while $A_{1-2x}Bi_{2x}B_{1-x}Me_xO_4$ compositions still have not been characterized well. However, similar coordination of ions and ionic radii ($r_{Ca^{2+}_{VIII}}$ = 1.12, $r_{Bi^{3+}_{VIII}}$ = 1.17 Å, $r_{Mo^{6+}_{IV}}$ = 0.41 Å, $r_{Ge^{4+}_{IV}}$ = 0.39 Å [12]) suggest existence of $Ca_{1-2x}Bi_{2x}Mo_{1-x}Ge_xO_4$ solid solutions. Bismuth germanates were also reported to be photocatalysts [13] and dielectrics [14]; therefore, $Ca_{1-2x}Bi_{2x}Mo_{1-x}Ge_xO_4$ solid solutions are expected to show similar characteristics. In the present paper, $Ca_{1-2x}Bi_{2x}Mo_{1-x}Ge_xO_4$ were synthesized and their structural features and microwave dielectric properties were investigated.

2. Experimental

The compositions of the general formula $Ca_{1-2x}Bi_{2x}Mo_{1-x}Ge_xO_4$ ($0.025 \le x \le 0.5$) series were synthesized by a conventional solid state method [9, 15] from $CaCO_3$ (99.0%, Reakhim), Bi_2O_3 (99.9%, Merck), GeO_2 (99.99%, Lanhit) and MoO_3 (99.5%, Reakhim) in the range of 600–900 °C.

X-ray powder diffraction data were obtained using a Bruker Advance D8 diffractometer with a VANTEC1 detector (Ni filtered Cu Kα radiation, θ/θ geometry) in the Ural-M center of the Institute of Metallurgy. The data were collected in the 2θ range of 5–80°, in the steps of 0.02° with an effective scan time of 200 s per step. Calculated X-ray density of each sample was compared with the pycnometric density of powder and the geometrical density of ceramic samples. The morphology of the obtained powders was studied using a TESCAN VEGA3 SBH scanning electron microscope (SEM); secondary electron and backscattered electron images were obtained.

Raman spectra were obtained for the $Ca_{1-2x}Bi_{2x}Mo_{1-x}Ge_xO_4$ series with a Horiba LabRam HR800 Evolution spectrometer including Edge filters and equipped with an Olympus BX-FM confocal microscope (50×objective, numerical aperture = 0.7) and a He–Ne laser (radiation wavelength 633 nm) and 1800 gr/mm grating. The spectral resolution was about 1 cm^{-1} and the spatial lateral resolution was about 2 μm. The spectra were fitted using a Gaussian-Lorentzian model. The UV-Vis spectra were obtained in the range 350–1100 nm using a Thermo Scientific Evolution 300 spectrophotometer equipped with an integrating sphere. Energy gaps for direct inter-band transitions were calculated through the linear approximation of the Kubelka-Munk function [16]. General increasing trends with increasing *x*-value are seen in the FWHM values (Figure S3) indicating a variation in the length of Mo–O bonds. However, the Raman spectra of $Ca_{1-2x}Bi_{2x}Mo_{1-x}Ge_xO_4$ were analyzed by traditional fitting and analysis of FWHM and by the analysis of the autocorrelation function (AAF). The autocorrelation function $Corr(\alpha,\omega')$ proposed by Salje et al. [17] is a way of parametrizing effective line widths in vibrational spectra to examine trends in similar samples. $Corr(\alpha,\omega')$ was calculated using Equation 1,

$$Corr(\alpha,\omega') = \int_{-\infty}^{\infty} \alpha(\omega+\omega')\alpha(\omega)d\omega, \quad (1)$$

where α(ω) is the primary spectrum and α(ω + ω ') is a replica of the spectrum shifted by ω'. The key parameter of AAF is the Δ*corr* parameter. The Δ*corr* is an approximation of the σ parameter of the Gaussian function, which is calculated from the *Corr(α, ω')*. By [17] it was calculated by following method: (1) the background was subtracted from the *α(ω)* initial spectrum, the $Corr(\alpha,\omega')$ was calculated and normalized; (2) the *Corr(α,ω')* peak apexes were approximated by the Gaussian function; (3) the Δ*corr* parameter was determined by extrapolating the *σ* function to $\Delta\omega' = 0$ point using second-order polynomials. In the present work we used a modified Gaussian function. The Δ*corr* is the average estimate of the FWHM of the peaks present in the analyzed part of the spectrum. In the present work *Δcorr* was calculated over three frequency ranges: 50–250 cm^{-1}, 250–550 cm^{-1} and 700–1000 cm^{-1}.

The electrodynamic parameters of the ceramic sample were measured by the transmission line method (Figure 1) using a vector network analyzer R&S ZVA50 [18]. A waveguide line of the WR90 type was used; the frequency range was from 8 to 12 GHz. Calculation of complex permittivity was carried out using specialized software [19]. The error in determining the permittivity is primarily determined by the basic error in measuring the modulus and phase of the transmission and reflection coefficient, S_{21} and S_{11}, respectively. An additional source of error is the non-ideal matching of the used elements of the transmission line on the amount of insertion loss. The electrodynamic properties of ceramic samples can be described by the coefficient of full reflection S_{11} and the transfer coefficient S_{21} measured by a vector network analyzer. Using these parameters, we had the possibilities for calculating the coefficient of reflection (*Γ*) and the coefficient of attenuation of electromagnetic waves in material (*Z*), from which, using the NRW mathematical model [20], we were able to calculate the complex permittivity of the sample under study.

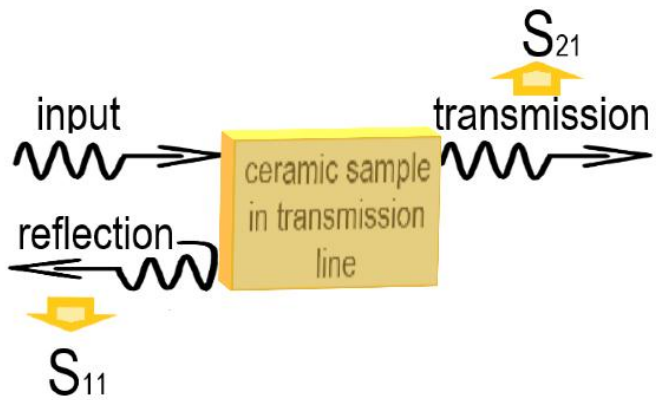

Figure 1 Diagram of EMW passage through the sample: wave falling on the surface of the sample, reflected and transmitted wave.

3. Results and Discussion

3.1. Synthesis

The X-ray diffraction patterns of representative compositions in the $Ca_{1-2x}Bi_{2x}Mo_{1-x}Ge_xO_4$ systems are shown in Figure 2. In the compositional range $0 \leq x \leq 0.4$ the patterns of $Ca_{1-2x}Bi_{2x}Mo_{1-x}Ge_xO_4$ can be indexed using a tetragonal scheelite model in the space group $I4_1/a$, with trace amounts of bismuth germanate or oxide phases (total quantity of impurity ≤1.4 wt.%, see Figure S1 and Table S1). XPRD patterns of the $x = 0.45$ composition also contain reflections from bismuth germanate or germanium oxides phases. The $BiMo_{0.5}Ge_{0.5}O_4$ ($x = 0.5$ composition) is a mixture of complex oxides with bismuth vanadates-type structures. SEM (Figure 3) shows the presence of trace amounts of bismuth germanates. A similar situation was observed for $Ca_{1-x}Bi_xMo_{1-x}V_xO_4$ series, where compositions were reported to be «basically single phase with a tetragonal crystal structure» in the range of $0.1 \leq x \leq 0.9$ [6], while a small amounts of Bi_2O_3 or $BiVO_4$ were detected [6, 20]. In these work, the authors indicated that a small quantity of the impurity phase could not significantly modify the physicochemical properties of the $CaMoO_4$-based solid solutions. So, we were following the same approach when we described physicochemical properties of $Ca_{1-2x}Bi_{2x}Mo_{1-x}Ge_xO_4$.

The compositional dependence of unit cell parameters is shown in Table 1. The values of X-ray density are close to the pycnometric density of powder samples. The geometrical density of ceramics is ~60–63% of the theoretical X-ray density. The porosity is relatively high (Table 1) but it slowly decreases with x.

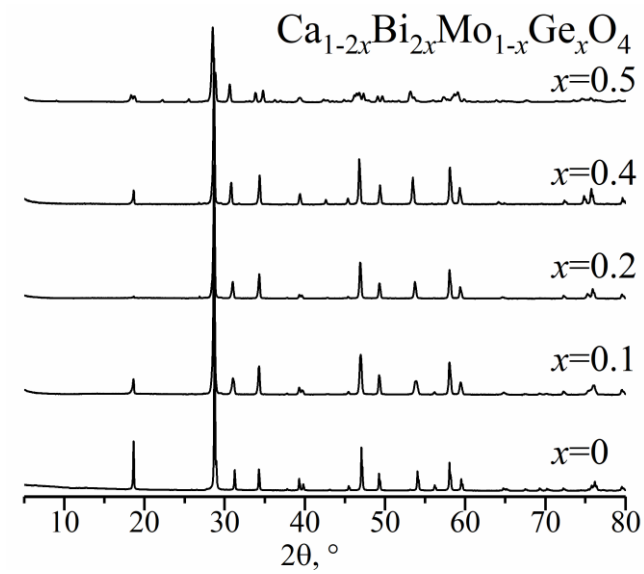

Figure 2 Detail of X-ray diffraction patterns of selected compositions of the $Ca_{1-2x}Bi_{2x}Mo_{1-x}Ge_xO_4$ systems.

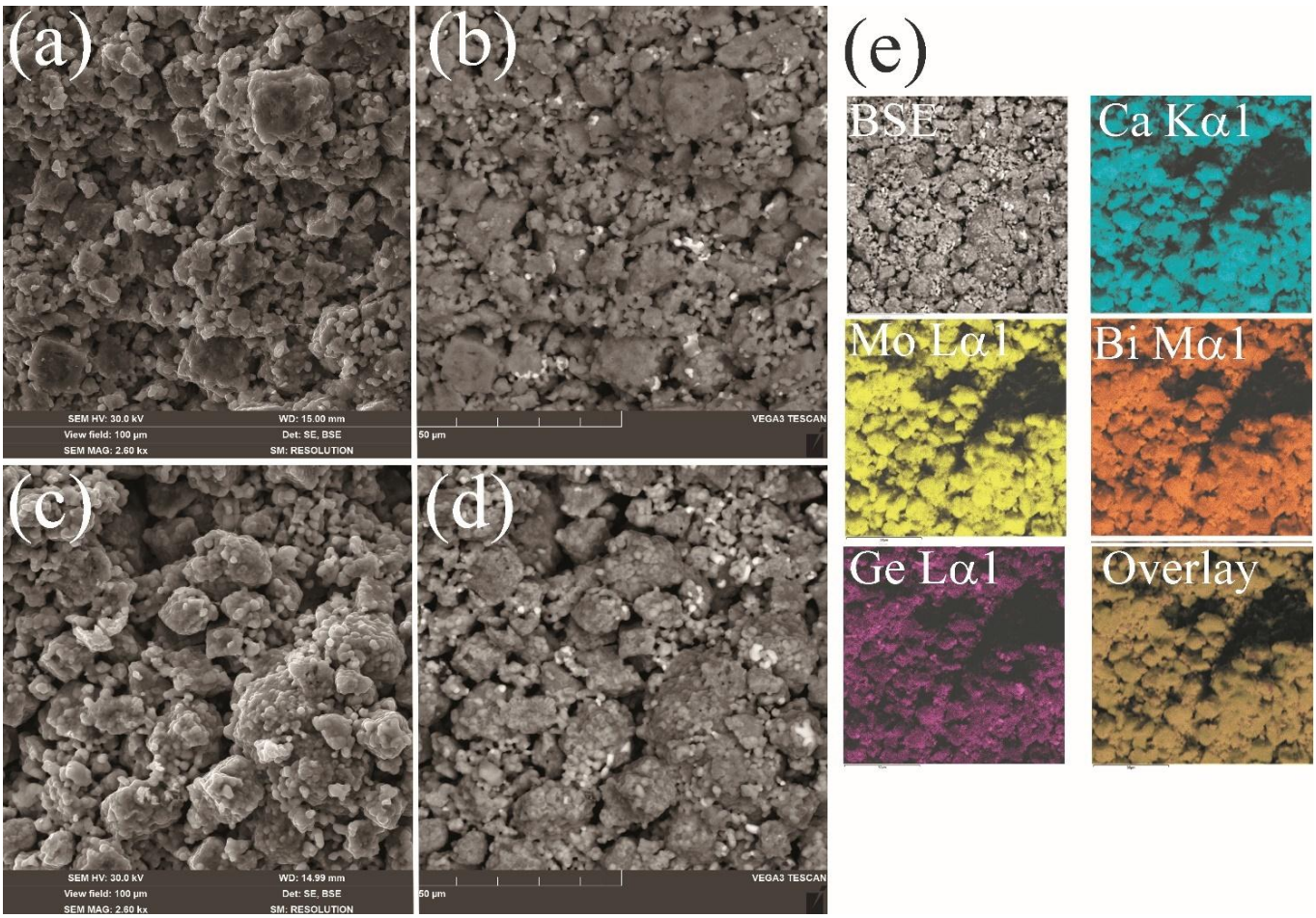

Figure3. SEM images of fracture surfaces of a ceramic pellet of $x = 0.1$ composition (a, b) and $x = 0.2$ composition (c, d): secondary electrons imaging (a, c); backscattering electrons (BSE) imaging (b, d); EDX-mapping + BSE of $x = 0.2$ composition, Ge-rich areas are detected (e).

Table 1 Unit cell parameters, unit cell volume, density values and E_g values of $Ca_{1-2x}Bi_{2x}Mo_{1-x}Ge_xO_4$ compositions.

x	*a*, Å	*c*, Å	*V*, Å³	X-Ray density, g/cm³	Density of powders, ±0.02g/cm³ and percentage of X-Ray density	Geometrical density of ceramic samples, g/cm³ and porosity%	E_g, eV
0.05	5.2242	11.4679	312.98	4.58	4.54/99.1	2.70/41	3.29
0.10	5.2242	11.4934	313.67	4.90	4.83/98.5	2.72/45	3.23
0.15	5.2245	11.5165	314.35	5.22	5.16/98.9	2.87/45	3.16
0.20	5.2245	11.5331	314.80	5.55	5.46/98.4	3.24/42	3.11
0.25	5.2238	11.5500	315.18	5.87	5.78/98.4	3.53/40	3.04
0.30	5.2229	11.5694	315.59	6.20	6.08/98.1	3.83/38	3.01
0.35	5.2213	11.5843	315.89	6.52	6.42/98.4	4.03/38	2.94
0.40	5.2190	11.6085	316.20	6.84	6.86/100	4.28/37	2.92

3.2. Vibrational spectroscopic studies

The examples of Raman spectra of $Ca_{1-2x}Bi_{2x}Mo_{1-x}Ge_xO_4$ are shown in Figure 4. $Ca_{1-2x}Bi_{2x}Mo_{1-x}Ge_xO_4$ ceramics are tetragonal scheelite solid solutions, whose structure is similar to that of $CaMoO_4$. Therefore, $Ca_{1-2x}Bi_{2x}Mo_{1-x}Ge_xO_4$ and $CaMoO_4$ have similar vibrational spectra. The vibration modes in $CaMoO_4$ include internal modes, which correspond to vibrations inside the $[MoO_4]^{2-}$ tetrahedra, and external modes that are assigned to lattice vibrations. As a result of crystal field effects and Davydov splitting, the degeneracy of the $[MoO_4]^{2-}$ vibrations corresponding to Td symmetry in free space is resolved.

The group theoretical analysis predicts that 26 modes are possible in the case of tetragonal scheelite-structured compounds in the space group $I4_1/a$, which are distributed as irreducible representations [1, 22–23]: $\Gamma = 3A_g + 5B_g + 5E_g + 5A_u + 3B_u + 5E_u$, of which the A_g, B_g and E_g vibrations are Raman active, whereas the A_u, B_u and E_u vibrations are infrared active. In this study, 13 vibrational modes are observed for the end member $CaMoO_4$, in good agreement with the previous experimental and calculated results for this composition [1, 22–23]. According to the previous studies on $CaMoO_4$-based systems, the peaks at low frequencies (modes 1–6 in Figure 4) correspond to the external modes of O–Mo–O and Ca–O bands [22–23]. The modes at medium and high frequencies are associated with the internal vibrations (modes 7–12). The Mo–O bending modes are located at medium frequencies (ν_2 and ν_4, modes 6–10) and the Mo–O stretching modes are detected at high frequencies (ν_1 and ν_3, modes 11–13) [22–23].

The incorporation of bismuth and germanium into $CaMoO_4$ leads to a broadening of the peaks in the Raman spectrum and the appearance of additional modes, viz.: mode-14 at 80–97 cm⁻¹, mode-15 at 451–455 cm⁻¹, mode-16 at 740–770 cm⁻¹, mode-17 at 890–900 cm⁻¹ and mode-13 at 80–97 cm⁻¹. Guo et al. assumed that the additional modes (at ~770–780, 820–880 and 910–930 cm⁻¹) in the Raman spectrum of $Ca_{1-3x}Bi_{2x}\Phi_xMoO_4$ indicated inequivalent Mo–O distances in distorted MoO_4 tetrahedra [23]. Similarly, in this work the additional mode-16 and mode-17 can be associated with distorted MoO_4 tetrahedra. According to the calculations on virtual crystals of $BiMoO_4$ and ΦMoO_4 in [24], the E_g mode-14 (80–97 cm⁻¹) can be described as the lattice mode and mode-15 can be described as the B_g ν_4 vibration of MoO_4. The additional mode-17 at 910–930 cm⁻¹ can be also ascribed to a short bond vibration in distorted or symmetrical MoO_4 tetrahedra. For example, such a mode was previously observed at ~929 cm⁻¹ for $SrMoO_4$ at high pressure (12 GPa) in [25] where $SrMoO_4$ had a distorted scheelite structure. Similar mode, in fact, was observed by Guo et al. [23] as can be seen in Figure 1 therein (the fitting was imperfect in the range of 900–1000 cm⁻¹).

General increase of full width at half maximum (FWHM) with increasing *x*-value is seen, indicating a variation in the length of Mo–O bonds. However, the Raman spectra are rather complex due to the intensive overlap of spectral lines observed in Figure 5a and FWHM vs *x* curves can not be plotted correctly. The compositional variation of some modes is shown in Figure 5b. Kanamori et al. [26] suggested that increase in the cation mass causes the vibrational frequencies of 'external' (lattice) modes to decrease in ABO_4 crystals. Generally, we observed this trend and deviation from trends indicated a closeness of solid solutions ranges. The analysis of the autocorrelation function (AAF) was carried out in over three frequency ranges (50–250 cm⁻¹, 250–550 cm⁻¹ and 700–1000 cm⁻¹, covering the lattice modes, $\nu_2 + \nu_4$ and $\nu_1 + \nu_3 + \nu_4$, respectively).

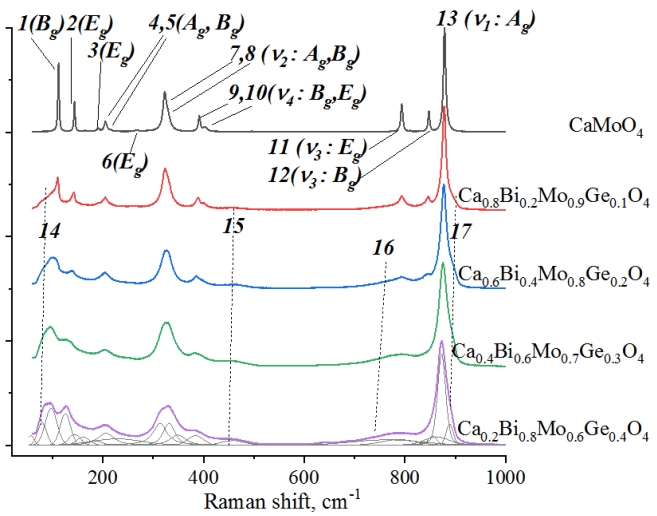

Figure 4 Raman spectra of selected compositions in the $Ca_{1-2x}Bi_{2x}Mo_{1-x}Ge_xO_4$ system.

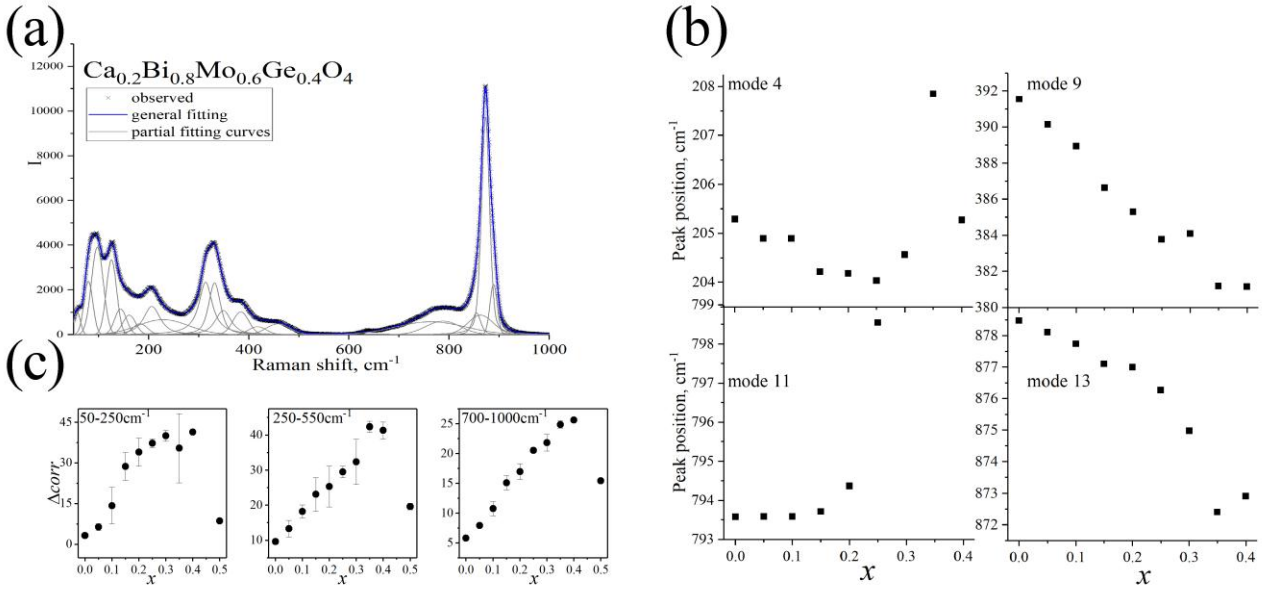

Figure 5 Raman spectra of $Ca_{0.2}Bi_{0.8}Mo_{0.6}Ge_{0.4}O_4$ powder, black crosses are experimental data and solid lines are the Gauss+Lorentz modes (a); compositional variation of wavenumber of Raman peak in $Ca_{1-2x}Bi_{2x}Mo_{1-x}Ge_xO_4$ compositions (b); *Δcorr* over three frequency ranges (50–250 cm^{-1}, 250–550 cm^{-1} and 700–1000 cm^{-1}) for $Ca_{1-2x}Bi_{2x}Mo_{1-x}Ge_xO_4$ compositions (c).

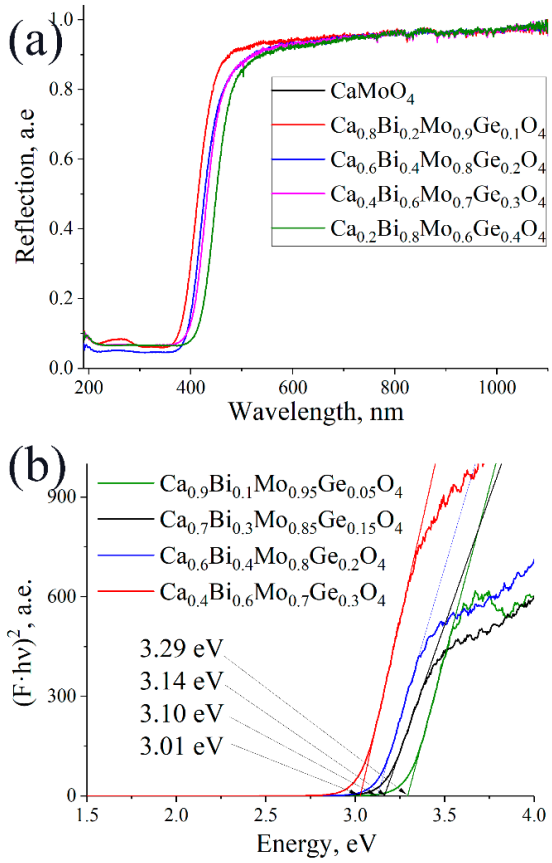

Figure 6 Optical diffuse scattering spectra for selected compositions in the $Ca_{1-2x}Bi_{2x}Mo_{1-x}Ge_xO_4$ system (a) and Tauc plots for the x == 0.05, 0.15,0.20 and 0.30 compositions (b).

For all wavenumber ranges, the Δ*corr* parameter (i.e. FWHM values) increases up to $x = 0.35–0.4$ indicating a solid solution area (Figure 5c). The $x = 0.5$ composition represents a sharp decrease of Δ*corr*, showing an end of the solid solution formation. Thus, these results are consistent with the XPRD data.

3.3. Diffuse scattering and energy gap

The optical diffuse scattering spectra of selected $Ca_{1-2x}Bi_{2x}Mo_{1-x}Ge_xO_4$ compositions are shown in Figure 6a. The scattering in the range of ~500–1100 nm is close to 100%. The spectra contain a broad band in the range of ~200–400 nm, which corresponds to electronic transitions within the molybdate tetrahedra [27]. In the substituted samples, this absorption band shifts to higher wavelength (Figure 6a). Band gaps (E_g) were calculated using the Kubelka-Munk theory and the Tauc relation (Figure 6b). E_g values decreased linearly with increasing x value (Table 1), ranging from 3.29 eV to 2.91 eV. Probably, the decrease in the band gap is provided by additional Bi 6p electrons in the valence band and changing of the conduction band, which includes Mo 4d and Ge 4p electrons. Such a band gap decrease is favourable for the use of these materials as yellow pigments or as photocatalysts, as in the case of the $Ca_{1-3x}Bi_{2x}\Phi_xMoO_4$ series [15].

3.4. Microwave dielectric properties

To study the electrodynamic properties of the $Ca_{1-2x}Bi_{2x}Mo_{1-x}Ge_xO_4$ samples, the measurements were carried out on rectangular ceramic plates, the dimensions of which correspond to the cross section of the waveguide transmission line used. The frequency dependence of the permittivity of several samples is shown in Figure 7. The average value of the permittivity increases with the bismuth content. For the composition with low dopant concentration ($x \leq 0.15$) the permittivity slightly changes in the frequency range of 8–12 GHz. An increase in the concentration of bismuth and germanium leads to the appearance of resonant peaks in the permittivity spectra and S_{11} permittivity S_{21} curves (Figure 8).When x increases, the frequency of the main peak decreases, and additional peaks appear. The

mechanisms for the formation of resonant peaks can include the appearance of structural domains containing only Bi atoms in the A position. Such domains due to the structural features of $6s^2$ isolated electrons, can be easily polarized by an external field of an electromagnetic wave. The increase in size of such domains is reasonably related to the increase in the bismuth concentration. Another source of resonances that appears on the permittivity curve can be a size of particles. In Figure 3 we can see that the size of particles increases with x increasing, which can lead to decreasing resonant frequency. The dielectric loss tangents (tan δ) of $Ca_{1-2x}Bi_{2x}Mo_{1-x}Ge_xO_4$ out of the resonant peaks are 0.01–0.07, which are reasonable magnitudes for dielectric materials. The average values of permittivity in the range of 8–12 GHz are shown in Figure 9 as ε_{exp}. The average permittivity ε_{obs} was calculated for polycrystalline data, but the relatively low sintering temperature leads to high porosity of ceramic samples, which is consistent with the previous works [4]. Thus, the dielectric constant in ε_{exp} was calculated from ε_{obs} by Equation 2:

$$\varepsilon_{exp} = \varepsilon_{obs}\,(1 + 1.5(P/100\%)), \qquad (2)$$

where P is the porosity and ε_{exp} is the measured dielectric constant [4]. The values of porosity (P) shown in Table 1 were determined using theoretical (X-ray) and experimental (geometrical) densities of ceramic samples.

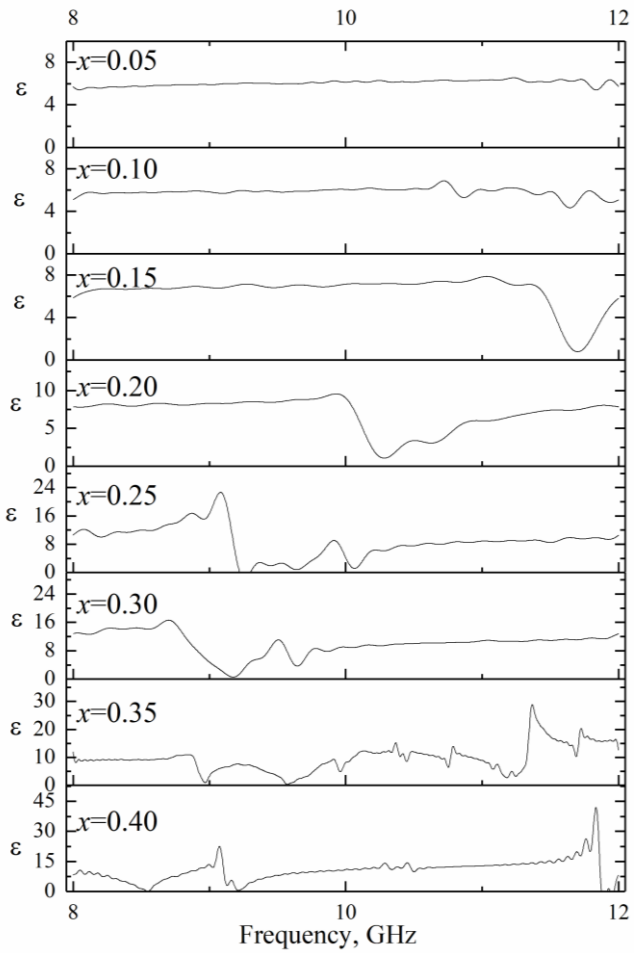

Figure 7 Permittivity spectra for selected compositions in the $Ca_{1-2x}Bi_{2x}Mo_{1-x}Ge_xO_4$ system.

Theoretical values of permittivity were calculated using the Shannon's suggestion [28] and Clausius–Mosotti equation. In the case of $Ca_{1-2x}Bi_{2x}Mo_{1-x}Ge_iO_4$ system, molecular polarizability can be estimated from Equation 3:

$$\alpha(Ca_{1-2x}Bi_{2x}Mo_{1-x}Ge_xO_4) = (1-2x)\cdot\alpha(Ca^{2+}) + (2x)\cdot\alpha(Bi^{3+}) + (1-x)\cdot\alpha(Mo^{6+}) + x\cdot\alpha(Ge^{4+}) + 4\alpha(O^{2-}), \qquad (3)$$

where α is the polarizability. The α values for all ions are 3.16, 6.12, 3.28, 1.63 and 2.01 Å^3 for Ca^{2+}, Bi^{3+}, Mo^{6+}, Ge^{4+}, O^{2-} ions respectively [4, 28]. Theoretical values of permittivity of $Ca_{1-2x}Bi_{2x}Mo_{1-x}Ge_xO_4$ could be calculated with polarizability from the Clausius–Mosotti relation (Equation 4):

$$\varepsilon_{theor} = \frac{3V_m + 8\pi\alpha}{3V_m - 4\pi\alpha} \qquad (4)$$

where V_m is the molar volume. Molar volumes of $Ca_{1-2x}Bi_{2x}Mo_{1-x}Ge_xO_4$ can be calculated with the unit cell parameters determined from the diffraction pattern and the values of molar units (Z). V_m, ε_{exp} and ε_{theor} are shown in Figure 9. As can be seen, the theoretical and experimental values of permittivity are close. The permittivity increases with x, which correlated with V_m changes and increase in $\alpha(Ca_{1-2x}Bi_{2x}Mo_{1-x}Ge_xO_4)$ due to the bismuth presence. Probably, the difference between ε_{exp} and ε_{theor} is caused by structural distortion, confirmed by Raman spectroscopy, and relatively low geometrical density of samples.

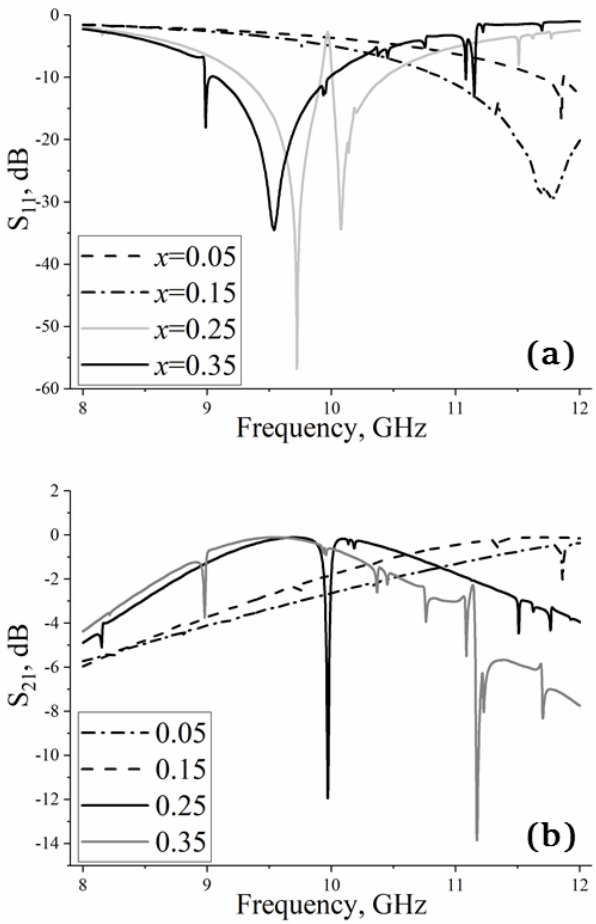

Figure 8 The dependences of the reflection coefficient S_{11} (a) and transmission coefficient S_{21} (b) on frequency for selected $Ca_{1-2x}Bi_{2x}Mo_{1-x}Ge_xO_4$ ceramic.

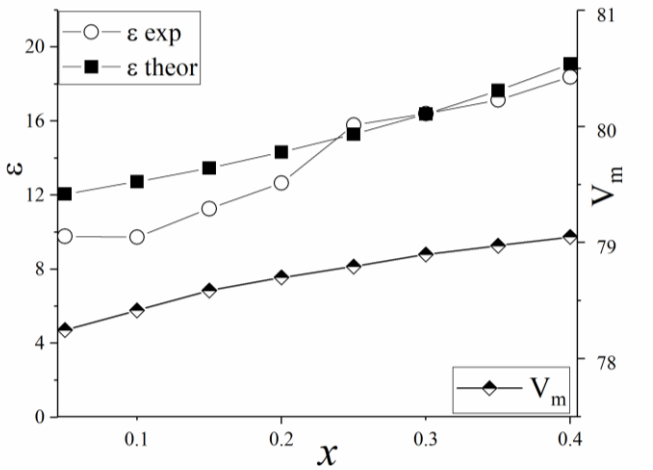

Figure 9 Molar volume, observed and calculated permittivity of $Ca_{1-2x}Bi_{2x}Mo_{1-x}Ge_xO_4$ compounds.

4. Conclusions

The $Ca_{1-2x}Bi_{2x}Mo_{1-x}Ge_xO_4$ complex oxides were synthesized by the conventional solid state method. X-ray powder diffraction showed that $Ca_{1-2x}Bi_{2x}Mo_{1-x}Ge_xO_4$ compositions crystalize in the scheelite structure at $0 \leq x \leq 0.4$, but traces of bismuth germanates were detected. Raman spectroscopy detected the deformation of $[BO_4]^{2-}$ polyhedra and changing of B–O bond length (B = Mo, Ge). Energy gap values calculated from diffuse scattering spectra decrease with *x*, probably, due to electrons of bismuth and germanium. E_g values of $Ca_{1-2x}Bi_{2x}Mo_{1-x}Ge_xO4$ show adsorption of visible irradiation, and it means that $Ca_{1-2x}Bi_{2x}Mo_{1-x}Ge_xO_4$ powders have to be tested as photocatalysts like another $CaMoO_4$-based compounds.

The electrodynamic parameters of the ceramic samples of $Ca_{1-2x}Bi_{2x}Mo_{1-x}Ge_xO_4$ were measured by the transmission line method. The main effects of bismuth and germanium doping of $CaMoO_4$ are (1) the increase of average permittivity of dielectric materials from ~10 to ~18 that correlates with theoretical ε, V_{mol} and total polarizability of samples; (2) the decrease of melting point with *x*, which results in the general simplification of the sintering processes; (3) the appearance of additional resonant peaks in the spectra of ε, S_{11} and S_{21}, which can be used in filtration system of microwave irradiation. Such resonant peaks can be probably caused by appearance of irregular structural domains of Bi atoms or induced by the increased size of grains in the ceramic samples. The dielectric loss tangents (tan δ) of $Ca_{1-2x}Bi_{2x}Mo_{1-x}Ge_xO_4$ out of resonant peaks are 0.01–0.07, which are reasonable magnitudes for dielectric materials.

We suggest that the $Ca_{1-2x}Bi_{2x}Mo_{1-x}Ge_xO_4$ system can be optimized by synthesizing the powders by wet-chemistry methods and forming the dense ceramic from such powders.

Supplementary materials

Supplementary materials are available.

Funding

This work was supported by the Russian Science Foundation (grant no. 20-73-10048), https://www.rscf.ru/en.

Russian Science Foundation

The Raman data were obtained in the Geoanalytic center of the Zavaritsky Institute of Geology and Geochemistry, UB RAS (re-equipment and comprehensive development of Geoanalytic is supported by the grant of the Ministry of Science and Higher Education of the Russian Federation (agreement No. 075-15-2021-680)).

Acknowledgments

The XRD data were obtained in the Ural-M center of the Institute of Metallurgy, UB RAS.

Author contributions

Conceptualization: Z.A.M., E.S.B.
Data curation: Z.A.M., E.S.B., E.A.P., A.I.M.
Formal Analysis: E.S.B., Z.A.M.
Funding acquisition: Z.A.M.
Investigation: Z.A.M., S.A.P., E.A.P., A.I.M, A.N.K., N.S.K.
Methodology: Z.A.M., E.A.P., S.A.P.,
Project administration: Z.A.M.
Resources: E.S.B.
Software: E.S.B., E.A.P., A.I.M.
Supervision: Z.A.M.
Validation: E.S.B., A.I.M.
Visualization: Z.A.M., E.S.B., A.I.M.
Writing – original draft: Z.A.M., E.S.B., A.I.M.
Writing – review & editing: Z.A.M., E.S.B., A.I.M.

Conflict of interest

The authors declare no conflict of interest.

Additional information

Author IDs:

Zoya A. Mikhaylovskaya, Scopus ID 26536460700;
Elena S. Buyanova, Scopus ID 26536460700;
Sofia A. Petrova, Scopus ID 7006291101;
Elizaveta A. Pankrushina, Scopus ID 57204032915;
Alexander I. Malkin, Scopus ID 57193847057;
Alexey N. Korotkov, Scopus ID 56439060500;
Nikolay S. Knyazev, Scopus ID 35090131500.

Websites:

Zavaritsky Institute of Geology and Geochemistry, http://eng.igg.uran.ru;
Ural Federal University, https://urfu.ru/en;
Institute of Metallurgy, http://www.imet-uran.ru.

References

1. Ramarao SD, Roopas Kiran S, Murthy VRK. Structural, lattice vibrational, optical and microwave dielectric studies on $Ca_{1-x}Sr_xMoO_4$ ceramics with scheelite structure. Mater Res Bull. 2014;56:71–79. doi:10.1016/j.materresbull.2014.04.064
2. Choi GK, Cho SY, An JS, Hong KS. Microwave dielectric properties and sintering behaviors of scheelite compound $CaMoO_4$. J Eur Ceram Soc. 2006;26(10–11):2011–2015. doi:10.1016/j.jeurceramsoc.2005.09.051
3. Guo HH, Zhou D, Pang LX, Qi ZM. Microwave dielectric properties of low firing temperature stable scheelite structure $(Ca,Bi)(Mo,V)O_4$ solid solution ceramics for LTCC applications. J Eur Ceram Soc. 2019;39(7):2365–2373. doi:10.1016/j.jeurceramsoc.2019.02.010
4. Choi GK, Kim JR, Yoon SH, Hong KS, Microwave dielectric properties of scheelite (A = Ca, Sr, Ba) and wolframite (A = Mg, Zn, Mn) $AMoO_4$ compounds. J Eur Ceram Soc. 2007;27:(8–9):3063–3067. doi:10.1016/j.jeurceramsoc.2006.11.037
5. Huerta-Flores AM, Juarez-Ramirez I, Torres-Martinez LM, Carrera-Crespo JE, Gomez-Bustamante T, Sarabia-Ramos O. Synthesis of $AMoO_4$ (A = Ca, Sr, Ba) photocatalysts and their potential application for hydrogen evolution and the degradation of tetracycline in water. J Photochem Photobiol A Chem. 2018;356:29–37. doi:10.1016/j.jphotochem.2017.12.029
6. Yao WF, Ye JH. Photophysical and photocatalytic properties of $Ca_{1-x}Bi_xV_xMo_{1-x}O_4$ solid solutions. J Phys Chem B. 2006;110(23):11188–11195. doi:10.1021/jp0608729
7. Pang LX, Zhou D, Liu WG, Qi ZM, Yue ZX. Crystal structure and microwave dielectric behaviors of scheelite structured $(1-x)BiVO_4 - xLa_{2/3}MoO_4$ (0.0 ≤ x ≤1.0) ceramics with ultra-low sintering temperature. J Eur Ceram Soc. 2018;38(5):1535–1540. doi:10.1016/j.jeurceramsoc.2017.10.051
8. Guo HH, Zhou D, Pang LX, Qi ZM. Microwave dielectric properties of low firing temperature stable scheelite structured $(Ca,Bi)(Mo,V)O_4$ solid solution ceramics for LTCC applications. J Eur Ceram Soc. 2019;39(7):2365–2373. doi:10.1016/j.jeurceramsoc.2019.02.010
9. Mikhaylovskaya ZA, Buyanova ES., Petrova SA, Klimova AV. ABO_4 type scheelite phases in $(Ca/Sr)MoO_4 - BiVO_4 - Bi_2Mo_3O_{12}$ systems: synthesis, structure and optical properties. Chim Techno Acta. 2021;8(2):20218204. doi:10.15826/chimtech.2021.8.2.04
10. Zhang GG, Fang QF, Wang XP, Yi ZG. Dielectric relaxation study of $Pb_{1-x}La_xMoO_{4+\delta}$ (x = 0–0.3) oxide-ion conductors. J Phys Condens Matter. 2003;15(24):4135–4142. doi:10.1088/0953-8984/15/24/307
11. Zhou D, Li WB, Guo J, Pang LX, Qi ZM, Shao T, Xie HD, Yue ZX, Yao X. Structure, phase evolution, and microwave dielectric properties of $(Ag_{0.5}Bi_{0.5})(Mo_{0.5}W_{0.5})O_4$ ceramic with ultralow sintering temperature. Inorg Chem. 2014;53(11):5712–5716. doi:10.1021/ic5004808
12. Shannon RD. Revised effective ionic radii and systematic studies of interatomic distances in halides and chalcogenides. Acta Cryst. 1976;A32:751–767. doi:10.1107/S0567739476001551
13. Ajiboye TO, Oyewo OA, Onwudiwe DC. The performance of bismuth-based compounds in photocatalytic applications. Surf Interfaces. 2021;23:100927. doi:10.1016/j.surfin.2021.100927
14. Ivanov MY, Nadolinny VA, Bagryanskaya EG, Grishin YA, Fedin MV, Veber SL. Bismuth germanate as a perspective material for dielectric resonators in EPR spectroscopy. J Magn Reson. 2016;271:83–89. doi:10.1016/j.jmr.2016.08.009
15. Mikhaylovskaya ZA, Abrahams I, Petrova SA, Buyanova ES, Tarakina NV, Morozova MV Structural, photocatalytic and electroconductive properties of bismuth-substituted $CaMoO_4$. J Sol State Chem. 2020;291:121627. doi:10.1016/j.jssc.2020.121627
16. Kubelka P, Munk FZ Ein beitrag zur optik der farbanstriche. Techn Phys. 1931;12:593–601.
17. Salje EKH, Carpenter MA, Malcherek T, Boffa Ballaran T. Autocorrelation analysis of infrared spectra from minerals. Eur J Mineral. 2000;12(3):503–519. doi:1127/0935-1221/2000/0012-0503
18. Malkin A, Chechetkin V, Korotkov A, Knyazev NC. Estimation of uncertainty of permittivity measurement with transmission line method in the wide frequency range. In: The 29th Telecommunications Forum TELFOR; 2021 Nov 23–24; Belgrade, Serbia. p. 1–3. doi:10.1109/TELFOR52709.2021.9653335
19. Malkin AI, Knyazev NS, Dielectric permittivity and permeability measurement system. In: Radio Electronics & Information Technologies REIT; 2017 March 15; Yekaterinburg, Russia. p. 45–51.
20. Nicolson AM, Ross GF. Measurement of the intrinsic properties of materials by time-domain techniques. IEEE Trans Instrum Meas. 1970;19(4):377–82 doi:10.1109/TIM.1970.4313932
21. Sameera S, Prabhakar Rao P, Divya S, Raj KV, Aju Thara TR. High IR reflecting $BiVO_4$–$CaMoO_4$ based yellow pigments for cool roof applications. Energ Buildings. 2017;154:491–98. doi:10.1016/j.enbuild.2017.08.089
22. Porto SPS, Scott JF. Raman Spectra of $CaWO_4$, $SrWO_4$, $CaMoO_4$, and $SrMoO_4$. Phys Rev. 1967;157(3):716–719. doi:10.1103/physrev.157.716
23. Guo J, Randall CA, Zhang G, Zhou D, Chen Y, Wang H. Synthesis, structure, and characterization of new low-firing microwave dielectric ceramics: $Ca_{1-3x}Bi_{2x}\Phi_xMoO_4$. J Mater Chem C. 2014;2(35):7364–7372. doi:10.1039/c4tc00698d
24. Mikhaylovskaya ZA, Pankrushina EA, Komleva EV, Ushakov AV, Streltsov SV, Isaac Abrahams I, PetrovaSA. Effect of Bi substitution on the cationic vacancy ordering in $SrMoO_4$-based complex oxides: structure and properties. Mater Sci Eng B. 2022;281:115741. doi:1016/j.mseb.2022.115741
25. Jayaraman A, Wang SY, Shieh SR, Sharma SK, Ming LC. High-pressure Raman study of $SrMoO_4$ up to 37 GPa and pressure-induced phase transitions. J Raman Spectrosc. 1995;26(6):451–455 doi:10.1002/jrs.1250260609
26. Kanamori H., Hayashi S, Ikeda Y. External lattice vibration Modes in scheelites. J Phys Soc Jpn. 1974;36 (2):511–516. doi:10.1143/JPSJ.36.511
27. Verma A, Sharma SK. Rare-earth doped/codoped $CaMoO_4$ phosphors: A candidate for solar spectrum conversion. Solid State Sci. 2019;96:105945. doi:10.1016/j.solidstatesciences.2019.105945
28. Shannon RD. Dielectric polarizabilities of ions in oxides and fluorides. J Appl Phys. 1993;73(1):348–66. doi:10.1063/1.353856